Journal of Materials Science & Technology 85 (2021) 30–43

Contents lists available at ScienceDirect

Journal of Materials Science & Technology

journal homepage: www.jmst.org

Research Article

Evaluation of hydrogen effect on the fatigue crack growth behavior of medium-Mn steels via *in-situ* hydrogen plasma charging in an environmental scanning electron microscope

Di Wan [a,*], Yan Ma [b,c], Binhan Sun [c], Seyed Mohammad Javad Razavi [a], Dong Wang [a], Xu Lu [a], Wenwen Song [b]

[a] *Department of Mechanical and Industrial Engineering, Norwegian University of Science and Technology, Richard Birkelands vei 2B, 7491, Trondheim, Norway*
[b] *Steel Institute (IEHK), RWTH Aachen University, Intzestraße 1, 52072, Aachen, Germany*
[c] *Max-Planck-Institut für Eisenforschung GmbH, Max-Planck-Straße 1, 40237, Düsseldorf, Germany*

ARTICLE INFO

Article history:
Received 25 June 2020
Received in revised form 29 October 2020
Accepted 14 December 2020
Available online 9 February 2021

Keywords:
Hydrogen embrittlement
Fatigue crack growth (FCG)
Electron channeling contrast imaging (ECCI)
Medium-Mn steel
Hydrogen plasma

ABSTRACT

Fatigue crack growth (FCG) tests were conducted on a medium-Mn steel annealed at two intercritical annealing temperatures, resulting in different austenite (γ) to ferrite (α) phase fractions and different γ (meta-)stabilities. Novel *in-situ* hydrogen plasma charging was combined with *in-situ* cyclic loading in an environmental scanning electron microscope (ESEM). The *in-situ* hydrogen plasma charging increased the fatigue crack growth rate (FCGR) by up to two times in comparison with the reference tests in vacuum. Fractographic investigations showed a brittle-like crack growth or boundary cracking manner in the hydrogen environment while a ductile transgranular manner in vacuum. For both materials, the plastic deformation zone showed a reduced size along the hydrogen-influenced fracture path in comparison with that in vacuum. The difference in the hydrogen-assisted FCG of the medium-Mn steel with different microstructures was explained in terms of phase fraction, phase stability, yielding strength and hydrogen distribution. This refined study can help to understand the FCG mechanism without or with hydrogen under *in-situ* hydrogen charging conditions and can provide some insights from the applications point of view.

1. Introduction

As a strong candidate for the third-generation advanced high-strength steels (AHSS), medium-Mn steels have attracted significant attention from both industry and academia due to their excellent combination of production cost and mechanical properties [1–3]. Usually medium-Mn steels consist of an ultrafine-grained (UFG) microstructure with face-centered cubic (FCC) austenite (γ), body-centered cubic (BCC) ferrite (α) and sometimes body-centered tetragonal (BCT) martensite (α') phases in different proportions. The characteristics of such microstructure can be tailored by intercritical annealing (IA) at different temperatures, which has a substantial influence on the material's mechanical performance [2,4,5]. By controlling the chemistry and the microstructure, multiple deformation mechanisms can be realized in medium-Mn steels, such as transformation-induced plasticity (TRIP) [6,7] and twinning-induced plasticity (TWIP) [5] effects. Until now most of the studies on medium-Mn steels have been focusing on the microstructure - tensile property relationship at the ambient environment. However, a critical problem limiting the use of such steels is the hydrogen embrittlement, given that hydrogen is ubiquitous and quite easy to be absorbed in the materials during processing and service.

Hydrogen embrittlement is a symptom of degradation of mechanical properties in metallic materials with the presence of hydrogen within the microstructure. The general performance is a reduction in the ductility and a transition in the fracture surface from dimples to brittle-like fractures, which might lead to premature or catastrophic failure of the structural components. Since the first report of this phenomenon on iron and steel by Johnson in 1875 [8], several hydrogen embrittlement mechanisms have been proposed. Among these mechanisms, hydrogen-enhanced decohe-

* Corresponding author.
E-mail address: di.wan@ntnu.no (D. Wan).

https://doi.org/10.1016/j.jmst.2020.12.069

sion (HEDE) [9–11], hydrogen-enhanced localized plasticity (HELP) [12–15], adsorption-induced dislocation emission (AIDE) [16–18] and hydrogen-enhanced strain-induced vacancy formation (HESIV) [19,20] are the popular ones. These mechanisms have been focusing on different microstructural levels ranging from atomic bonds, vacancies, interstitial atoms to dislocations and grain boundaries to explain the unexpected behavior when hydrogen is present. A relatively new concept called "Defactant" (from DEFect ACTing AgeNT) [21–23] has also been proposed to describe the effect of hydrogen on dislocations behavior via thermodynamical calculations and successfully explained some hardening consequences in hydrogenated steels. However, due to the complexity of the phenomenon itself, no single mechanism is working for all the observed phenomena yet. More and more studies on different materials including iron, steels, nickel-based alloys and some other high-strength metallic materials have shown the complication of the hydrogen-induced degradation behavior. In some recent studies, the synergistic effect of different mechanisms, such as HELP + HEDE mechanism and HELP-mediated HEDE models, on hydrogen embrittlement has been investigated [24,25]. To better understand the proposed physical mechanisms and their interplay, therefore, it is highly demanding to reveal the real-time microstructural evolution during deformation of the materials in a hydrogen-containing environment [26–31].

Considering the hydrogen embrittlement of medium-Mn steels, only a limited number of reports has been presented so far. In 2012, Ryu et al. [32] studied the hydrogen desorption behavior in a TRIP-assisted steel with approx. 5 wt.% Mn, stating that the γ to α' phase transformation reduces the binding state of hydrogen and thus enhancing the hydrogen mobility which consequently leads to mechanical degradation. Han et al. [33] observed the tensile behavior of a medium-Mn TRIP-assisted steel (with approx. 7 wt.% Mn) after intercritical annealing, and correlated the fracture features with the microstructures based on the explanation by HEDE and HELP mechanisms. Jeong et al. [7] found that the morphology of austenite grains influences the hydrogen embrittlement susceptibility of medium-Mn steels due to the migration of hydrogen between the grains. Lu et al. [34] used advanced *in-situ* electrochemical nanoindentation (ECNI) technique to investigate the hydrogen influence on the nanomechanical behavior of a duplex medium-Mn steel and found that hydrogen reduces the stacking fault energy (SFE) of austenite, enhancing the slip planarity in the investigated material. Shen et al. [35] investigated microstructural influence on the hydrogen embrittlement susceptibility via tensile tests and Sun et al. [36] deepened the study to dislocation level and proposed the possible mechanisms inside grains.

The above brief review shows that most of the previous studies are focusing on the monotonic loading conditions. However, considering the possible loading conditions in the potential applications, the evaluation of hydrogen effect under a cyclic loading condition is also necessary. From a scientific point of view, the hydrogen-induced failure during tensile testing is a combined result of damage initiation and propagation. The influence of hydrogen on each individual stage of damage evolution in medium-Mn steels thus remains unclear. Further, post-mortem damage analysis on the fractured samples often shows that these hydrogen-induced damages are accompanied by γ to α' phase transformation (i.e. TRIP effect) [36]. However, such analysis is unable to address whether the martensite formation occurs before or after damage nucleation. These ambiguous points reflect a highly challenging task to unveil the detailed influence of H in multiphase TRIP-aided medium-Mn steels. Such analyzing challenges can be evaded by using a pre-cracked specimen. In such a case the crack initiation procedure can be strategically ignored since a pre-crack has been introduced and only crack propagation is considered. Besides, the retained γ phase can easily transform into α'-martensite, especially in the crack wake, due to the metastability of the γ phase [2,6,7,33,35–41] and the enhanced stress triaxiality and local strain at the crack tip area [42]. This early phase transformation before crack arrives simplifies the analysis from a complicated γ+α+possible α' TRIP multi-phase case to a relatively simple α+α' case.

Table 1
Chemical composition of the investigated medium-Mn steel (wt%).

Fe	C	Si	Mn	P	S	Al
balance	0.064	0.2	11.7	0.006	0.003	2.9

In the present work, we focus on the influence of hydrogen on crack propagation behavior in medium-Mn steels with different phase morphologies and austenite mechanical stabilities under a cyclic loading condition. The *in-situ* fatigue crack growth (FCG) behavior under both vacuum ($<10^{-5}$ Pa) and hydrogen-containing environment was investigated. The latter was realized by *in-situ* hydrogen plasma charging in an environmental scanning electron microscope (ESEM). A single specimen was loaded cyclically in different environmental conditions such that the behavior could be directly compared. The mechanical performance, fracture features and microstructure evolution were intensively analyzed, and the possible hydrogen embrittlement mechanisms were discussed. By using this experimental setup, the current study becomes fundamentally different from conventional pre-charged monotonic tensile tests. *In-situ* hydrogen charging provides a continuous hydrogen source that keeps influencing the FCG behavior and hydrogen (re-)distribution. Cyclic loading for FCG keeps the focus only at the crack propagation stage such that complexities from crack initiation can be simply ignored.

2. Materials and experimental

The as-received medium-Mn steel has a chemical composition as shown in Table 1. The laboratory-melt ingots were subjected to the processing history of hot rolling at 1150 °C, homogenization at 1100 °C for 2 h, austenitization at 850 °C for 10 min, cold rolling with 50% reduction in thickness, as described previously in Ref. [2]. The cold-rolled material was intercritically annealed at 555 °C and 700 °C for 12 h followed by water quenching. According to the IA temperature, the specimens are referred to as IA555 and IA700 hereafter. The IA555 batch shows a dual-phase microstructure consisting of α-ferrite and γ-austenite with a laminated morphology, while the IA700 batch mainly shows a recrystallized morphology with equiaxed α-ferrite and γ-austenite [2]. Quantitatively, the IA555 has ~42.2 vol.% γ phase and the IA700 has ~58.4 vol.% γ phase. The microstructure and phase fraction data can be found in Ref. [2]. In accordance with previous uniaxial tensile tests, the IA555 has a yield strength (0.2% offset yield strength) of about 899 ± 15 MPa and an ultimate tensile strength (UTS) of about 936 ± 16 MPa; while the IA700 has a yield strength of about 426 ± 14 MPa and an UTS of about 805 ± 30 MPa. The total elongation is ~17.0% ± 0.7% and ~33.5% ± 1.3% for IA555 and IA700, respectively [2].

Single-edge notched tensile (SENT) specimens are manufactured from the raw materials by water-jet cutting according to the sketch in Fig. 1(a). The SENT specimens were prepared by grinding to #2000 silica paper and final finishing by electropolishing in a H_2SO_4-methanol electrolyte at 18 V, 60 s for both sides. After preparation, no significant deformation from sample preparation could be observed. The pre-crack was initiated by cyclic loading in the tensile direction with a frequency of 60 Hz, load ratio[1] R = 0.1 far below the nominal yielding strength (maximum load lower

[1] The load ratio R is defined as the ratio between the minimum load (P_{min}) and the maximum load (P_{max}) during one loading cycle, *i.e.* $R = P_{min} / P_{max}$.

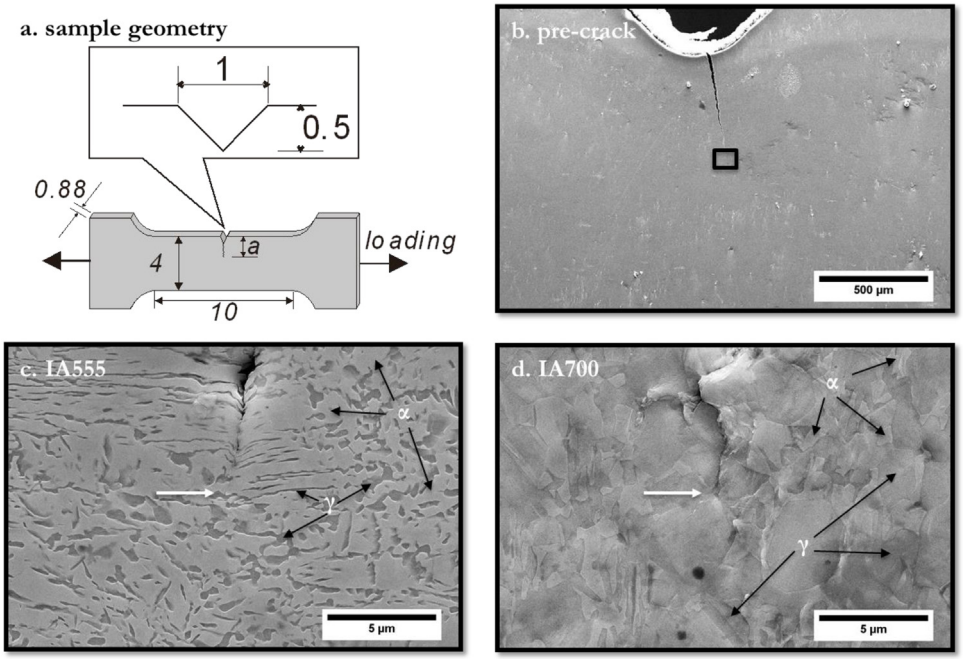

Fig. 1. (a) Schematic of the SENT specimen (unit: mm); (b) an exemplary image showing the pre-crack grown from the notch root (from IA700); (c) and (d) the pre-crack tip indicated by white arrows and the surrounding microstructure for IA555 and IA700, respectively.

than half of the nominal yielding strength). Such a small load for pre-crack initiation constrains the plasticity around the pre-crack tip. It should be noted that the mechanical data for crack initiation (the pre-cracking procedure) is not the topic of this paper and will not be discussed further. The pre-crack has a length of about 1 mm. An exemplary scanning electron microscope (SEM) image is shown in Fig. 1(b). The pre-crack tip region (as indicated by the black rectangular in Fig. 1(b) was further investigated at higher magnification, and Fig. 1(c) and (d) shows the exemplary cases for IA555 and IA700, respectively. The fatigue pre-crack was kept sharp in both cases, and no apparent plastic deformation was observed from the topography. The microstructure was similar to the report of Ref. [2], which exhibited a dual-phase structure as designed by the heat treatment procedures.

The cyclic loading was applied by a tensile/compression module (Kammrath & Weiss GmbH, Germany) inside an ESEM (Thermo Fisher Scientific Inc., USA) with a load ratio of R = 0.5 starting from a stress intensity range (ΔK) of about 6 MPa $m^{1/2}$. The tensile/compression module was operated in a load-controlled mode (load precision of 0.1 N) with a fixed displacement rate at 20 μm/s in both loading (tensile) and unloading (compression) directions, corresponding to a loading frequency of about 0.3 Hz. After every 100 cycles, the specimen was unloaded to 0 N for imaging to avoid possible elastic influences (i.e. the FCG test was periodically interrupted after each 100 cycles). The ESEM was operated at an acceleration voltage of 20 kV and both secondary electron (SE) images and backscatter electron (BSE) images were recorded. The stress intensity in the present work was calculated based on the SENT specimen assumption from Ref. [43]. The crack length was measured after every 100 cycles from the SEM images and the average FCGR was calculated by the crack length increment over the 100 cycles. The load value could be directly read from the tensile/compression module via the DDS software, and the K as well as the ΔK values were determined based on the load from the module and the measured crack length. The detailed calculation of K is introduced in Section 3.1.

For hydrogen charging, an Evactron plasma source (XEI Scientific Inc., USA) was used to ignite and inject the H-plasma phase into the ESEM chamber. The source hydrogen gas comes from a hydrogen generator based on the electrolysis of pure water. According to a report from the XEI Scientific Inc. [44], the resulting hydrogen radicals contained both hydrogen atoms and excited hydrogen gas molecules. A partial pressure of about 40 Pa was recorded during the charging procedure. The fugacity of hydrogen in the vicinity of the crack tip was estimated to be in the magnitude of megapascal (MPa) [45]. This charging method has been proven to be successful in charging ferritic steels and dual phase steels for hydrogen embrittlement study [46–48]. The environmental conditions are denoted as either Vac (in high vacuum) or H (in hydrogen plasma environment) hereafter. For each specimen, several Vac-H-Vac-H alternations were conducted to confirm the reproducibility of the hydrogen embrittlement behavior via this methodology. It is worth noting that the hydrogen uptake procedure in this methodology is not necessarily an ingression through the infinitesimal gap between the crack surfaces, but rather a diffusion into surface plus a redistribution near the crack tip due to the changing stress field. Such scenarios can also be seen in some fatigue crack growth tests with *in-situ* hydrogen charging methods such as electrochemistry [49–52] and high-pressure hydrogen gas [53–56]. It is worth mentioning that the nature of hydrogen residing in transition metals (such as Fe) has been discussed since decades ago, focusing on whether hydrogen is present as neutral atom, H^+ or H^- [57]. To avoid controversy, the current study does not differentiate the nature of hydrogen in the metals but focuses on the effect of hydrogen on the mechanical performance of the metals.

After the final failure, fractography was first studied by SEM at different magnifications. Then the fracture surfaces of the specimens were coated by electrodeposition of Ni to avoid losing the material due to the non-uniform removal at the edges during further sample preparation. Electron channeling contrast imaging (ECCI) was conducted in the same ESEM by the BSE detector. This technique allows to characterize crystallographic defects with a high-resolution up to individual dislocation level in bulk specimens including the investigated alloy system [52,58–60].

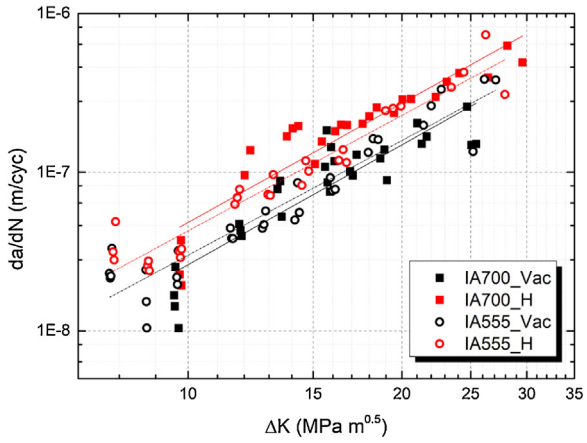

Fig. 2. Fatigue crack growth rate (FCGR) diagram of the tested IA555 and IA700 specimens in Vac and H conditions. Fitted lines are shown as solid and dashed lines for IA700 and IA555, respectively. Black lines show the data in vacuum condition and red lines show the data in hydrogen-charged condition. (digital version in color).

3. Results

3.1. Mechanical performance

A mode I crack (opening mode) was assumed through the whole test, whose stress intensity can be calculated as Eq. (1):

$$K_I = \frac{P}{B\sqrt{W}} f\left(\frac{a}{W}\right) \quad (1)$$

where P is the load, B and W are the thickness and width of the specimen, respectively; a is the crack length as can be read according to Fig. 1(a) and f is a dimensionless function which is defined as Eq. (2) [43]:

$$f\left(\frac{a}{w}\right) = \frac{\sqrt{2tan\frac{\pi a}{2W}}}{cos\frac{\pi a}{2W}}\left[0.752 + 2.02\left(\frac{a}{W}\right) + 0.37\left(1 - sin\frac{\pi a}{2W}\right)^3\right] \quad (2)$$

The stress intensity range (ΔK) is thus calculated as Eq. (3):

$$\Delta K = K_{max} - K_{min} \quad (3)$$

where K_{max} and K_{min} are the maximum and minimum K_I values during one loading cycle, respectively.

Fig. 2 shows the fatigue crack growth rate (FCGR) - ΔK curves in logarithmic scale of the tested specimens in both Vac and H conditions. Clearly, the data points indicate a relatively good reproducibility of the testing results in both conditions. This reproducibility should be understood from the following points. The data points were from a test on a single specimen under changing environmental conditions (Vac-H alternatively). When the environment was changed from Vac to H, the FCGR increased; when the environment was changed from H to Vac, the FCGR decreased back to the original level. This change was repeatable during the whole test sequence. Two materials (i.e. IA555 and IA700) with the same sample geometry were tested, and the results are slightly different, meaning that the difference was not from a systematic error from the tensile module but due to different materials behavior. These points together can validate the experimental setup on studying the environmental (hydrogen plasma) effect and the reproducibility of the results. In Vac, the IA555 specimen had a slightly higher FCGR than IA700 when ΔK was below 10 MPa $m^{1/2}$, but the FCGRs of both materials approach to a similar level as ΔK increases. In H, both the two materials showed an increased FCGR, but to a different extent and the IA700 showed a generally higher FCGR than IA555 in the hydrogen-charged condition.

Table 2
The fitted C and m constants according to Paris' law.

Material	Environment	C	m
IA555	Vac	4.89×10^{-5}	2.40
	H	5.61×10^{-5}	2.41
IA700	Vac	4.13×10^{-5}	2.51
	H	5.48×10^{-5}	2.50

The stable crack growth regime can be described by the Paris' law [61]. The basic mathematical presentation is shown in Eq. (4):

$$\frac{da}{dN} = C(\Delta K)^m \quad (4)$$

where da/dN is the crack growth rate per cycle, C and m are constants based on the materials and testing conditions. Based on this mathematical relation, a linear relation can be expected in a logarithmic plot.

The data points in Fig. 2 were fitted according to Eq. (4) and the fitted lines are shown as solid and dashed lines for IA700 and IA555 specimens, respectively. Table 2 shows the fitted C and m constants. It can be seen that in the hydrogen environment, the C value increased from 4.89×10^{-5} to 5.61×10^{-5} (by 7.2×10^{-6}) for the IA555 case and from 4.13×10^{-5} to 5.48×10^{-5} (by 1.35×10^{-5}) for the IA700 case, respectively. Clearly, the effect of hydrogen on increasing the FCGR is more pronounced in the IA700 sample than that in the IA555 sample. The fitted m values in Table 2 denote the slopes of the curves in Fig. 2. For both materials, a similar m value was found in the cases with and without hydrogen-charging, meaning the acceleration of FCGR was a "parallel" acceleration over the tested ΔK range on logarithmic scale. In the studied environmental condition of 40 Pa hydrogen plasma, at a same ΔK level, the IA555 specimen had a FCGR of about 1.7 times of that in Vac, while the IA700 specimen had a FCGR of roughly 2 times of that in Vac. As a summary, this dataset means a higher hydrogen embrittlement susceptibility of the IA700 material than the IA555 material. It is worth noting that an error can be expected in the accurate determination of the ΔK level and the FCGR rate. However, the focus of the current work is to study the susceptibility of hydrogen-assisted FCGR in the two medium-Mn steels, and for each test, at least nine (9) repetitions (i.e. changing environment from Vac to H) were conducted, in which all of them showed the same effect of acceleration of FCGR in the hydrogen environment compared with that in vacuum for both materials. Therefore, a good reproducibility of the hydrogen-assisted FCGR is confirmed, although the global acceleration factor of 2 times or 1.7 times is not surprisingly high.

It is not redundant to say that the data measured in Fig. 2 and Table 2 are valid in the current work to show the hydrogen-assisted FCG behavior. Any attempt to compare the mechanical properties with other conventional tests using different samples geometries or different loading systems in ambient conditions needs to be further validated before the assessment.

3.2. Crack morphology

The crack morphologies were recorded by SEM periodically after every 100 cycles. Fig. 3 shows the situation for the tested specimens at a low ΔK level (9.6-9.7 MPa $m^{1/2}$). The yellow arrows indicate the crack growth path from the last 100 cycles with the necessary information added in the figure. Upon cyclic loading, the crack growth is normally accompanied by the plastic deformation in terms of topographical change at areas near the crack. After loading, some topographical roughness is still visible near the closed crack tip. The apparent deformation zones in the form of material pile-ups are marked by black arrows in Fig. 3. For both samples, it is noted that the topographical change is more pronounced when crack propagates in the Vac environment, compared with its prop-

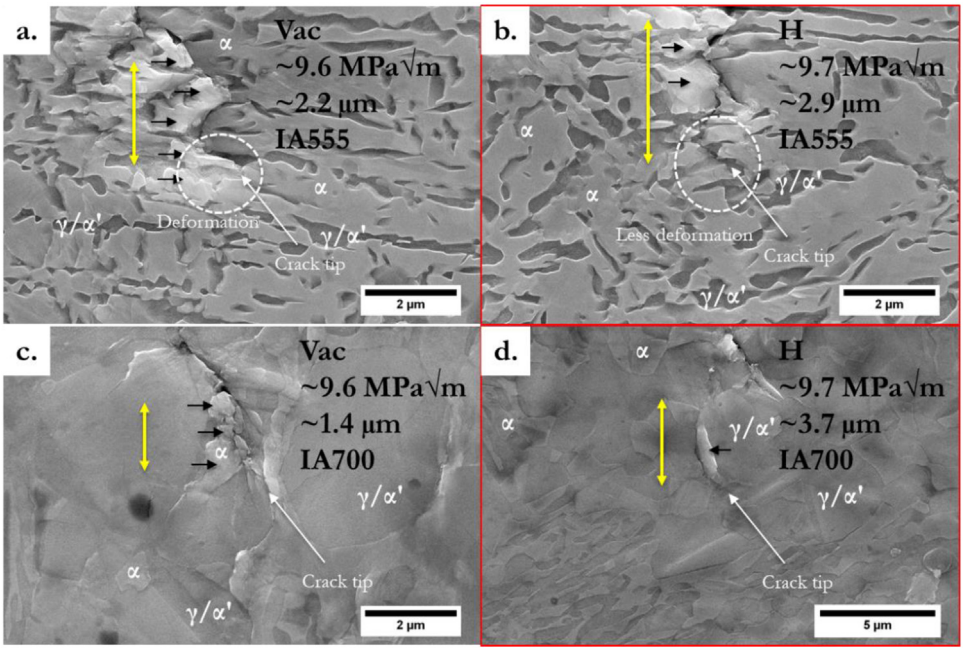

Fig. 3. Crack morphologies at a low ΔK level: (a, b): IA555 crack grown in Vac and H, respectively; (c, d): IA700 crack grown in Vac and H, respectively. The magnifications for c and d are NOT the same. The yellow arrows indicate the crack growth path for the last loading of 100 cycles. The information in the figures shows the environmental condition, ΔK level, crack growth length and the material. (digital version in color).

agation in the H environment. Such observation indicates that with the presence of H, less plastic deformation is created during crack propagation in both samples, i.e. the materials are embrittled by H. Another interesting fact is that in the IA555 specimen, the crack was growing across the γ/α' phase mostly in a transgranular (TG) manner, regardless of the testing environment. Especially in Fig. 3(b), the crack tip shows a clear path in the γ/α' phase and no significant intergranular (IG) fracture is visible. In contrast to the IA700 sample, the crack path shows mainly TG cracking in Vac, while in hydrogen, a mixed type of both TG and IG cracking can be observed. It is worth mentioning that differentiating γ and deformation-induced α'-martensite in the studied material with such a UFG microstructure is challenging by SE imaging. Based on the experience of the authors [4,36,39,40,60,62,63], the γ phase close to the fatigue crack tip can easily transform into α'-martensite during crack propagation due to the locally high stress and strain fields (usually at nanometer to micrometer scale), and the crack propagation happens after the α'-martensitic transformation. However, due to the resolution of the current techniques, the local γ and α' phases are not differentiated.

Figs. 4 and 5 show long-term observation of the FCG of IA555 and IA700 in different environmental conditions, respectively. The sub-figures were stitched from the *in-situ* images similar as in Fig. 3. Since these images were taken after unloading to 0 N, the fatigue crack tip has already been closed during imaging. In Figs. 4 and 5, crack propagation stages at different atmospheres (Vac and H) are divided by dashed lines and the arrows point the crack tip at the end of each propagation stage. The corresponding mechanical data (ΔK level and crack growth length) is also added on the right side of each sub-figure. Each complete crack propagation stage (the region between two nearby dashed lines) corresponds to a loading period of 300 cycles in total. For both samples (Figs. 4 and 5), a clear fact is that the loading in hydrogen environment led to a longer crack growth path in comparison with the Vac condition, which supports the promoting effects of hydrogen on crack propagation. (*N.B.* the last H sections in Figs. 4(d) and 5 (d) are not from a complete 300-cycle-loading but only a 100-cycle-loading due to the limit of the figure size.) The winkle-like pile-ups near the crack path are more significant in the Vac case while they are less visible in the H case. In contrast to IA555, IA700 shows a clearer transition in the shape of the crack path when the testing environment has been changed. In Vac, the crack was growing in a roughly straight manner, corresponding to the perpendicular direction of the cyclic loading; while in hydrogen, a zigzag growth path can be seen, which could correspond to the local grain boundary distribution. This phenomenon provides a sign that the dominant crack growth mode was shifted from a TG manner to an IG manner by the introduction of hydrogen, and comparing the two materials, the IA700 seems to have a higher fraction of the IG fracture than that of IA555. The observations in Figs. 4 and 5 are in good agreement with the observations at a finer scale (Fig. 3) and at the global mechanical performance level (Fig. 2), showing a good reproducibility of the present test. It is worth mentioning that the Figs. 4 and 5 are presented at a lower magnification to show the global crack growth history, and the ultra-fine features of the studied materials cannot be clearly differentiated. For higher-magnified features, the readers are suggested to correlate with the characterization results in the latter sections of the paper.

3.3. *Fractography*

After cyclic loading, the specimens were continuously loaded by monotonic tensile loading to fracture, and the fractographs were probed by SEM. Fig. 6 shows an overview of the fracture surfaces from the tested specimens. By correlating to the crack length data from the *in-situ* top-surface investigation, the fracture surface resulting from crack propagation through alternative environmental conditions can be identified. A common feature for these two specimens is that some microvoids or dimple-like structures are generally observed in most places, both in Vac and H environments. They appear both in the fatigue regions at different ΔK levels and in the monotonic loading regions. Such features show a globally ductile performance of the tested materials under both monotonic and cyclic loading conditions and the failure is mainly realized by microvoid coalescence mechanisms, especially in the final fracture part. Fig. 6(a_1) and (a_2) show the magnified features

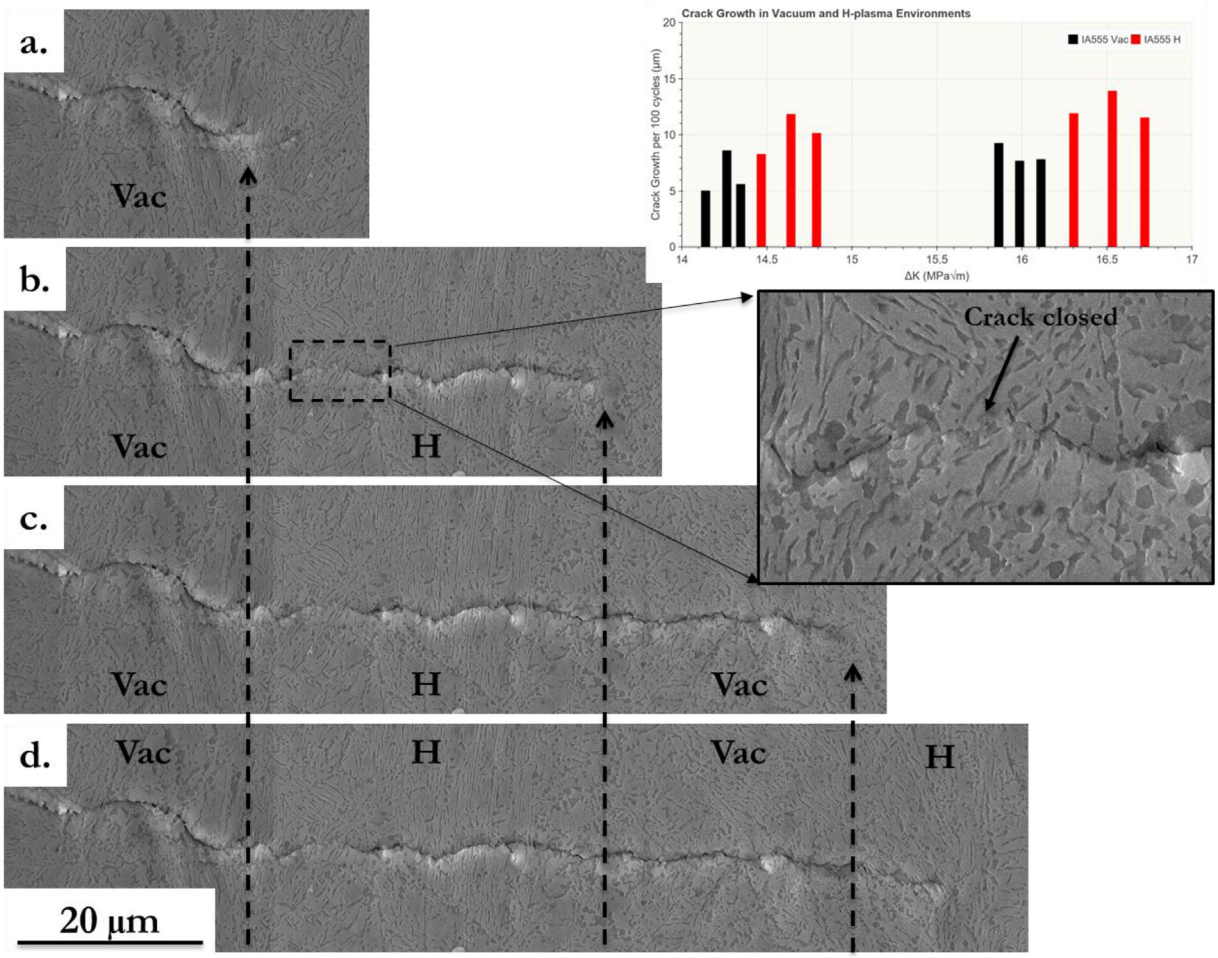

Fig. 4. Long-term crack morphology observation of IA555. The crack growth data from the presented region is shown in the bar chart. The global FCG direction is from left to right. The figures are stitched to show the crack growth history.

in the regions fractured in the Vac and H environments shown in Fig. 6(a), respectively. In Vac, the IA555 specimen shows a general TG type FCG, fatigue striations as well as some microvoids (MVs) can be observed in the magnified images (Fig. 6(a_1)). In comparison, secondary cracks become a distinct feature in H even though the general FCG still manifests a TG type (Fig. 6(a_2)). Similarly, Fig. 6(b_1) and (b_2) shows the detailed microstructures in the IA700 specimen in Fig. 6(b). In Vac, the IA700 specimen shows a similar TG type FCG with MVs on the fracture surface (Fig. 6(b_1)). When the environment was changed to hydrogen, some IG type features as well as "quasi-cleavage" ("QC") features appear as typical features on the fracture surface (Fig. 6(b_2)).

For the IA555 specimen, the fracture surface at a higher magnification (Fig. 7) appears ductile and TG in Vac (Fig. 7(a)), while in the H case, facets in the size of about 10 μm can be generally observed (Fig. 7(b)). The ductile fracture in the Vac case consists of dense fatigue striations nearly perpendicular to the global FCG directions (Fig. 7(c)). In contrast, the striations in the H case at the same ΔK level of about 26 MPa $m^{1/2}$ are associated with secondary cracks (Fig. 7(d)) and the distance in between is larger than that in the Vac case (~0.12 μm/cyc in Vac vs. ~0.39 μm/cyc in H, determined by the distance over at least 20 striations in more than three different locations of each condition). No clear IG or cleavage/ "QC" fracture features have been observed in the IA555 sample, even in the presence of hydrogen.

Fig. 8 shows the detailed fracture surface of the IA700 specimen. At a relatively lower magnification (Fig. 8(a) and (b)), the fracture surfaces look ductile and MVs can be generally seen in both Vac and H cases at a similar ΔK of about 20 MPa $m^{1/2}$. At a higher magnification (Fig. 8(c)and (d)), again strong difference can be observed between Vac and H cases. In Vac case (Fig. 8(c)), the fracture surface contains dense fatigue striations appearing on the ridges. The fracture surface still looks rounded either with or without striations. In H case (Fig. 8(d)), however, the distance between the striations is larger than the case in Vac, indicating a faster FCGR within a single cycle (~0.13 μm/cyc in Vac vs. ~0.28 μm/cyc in H, determined by the distance over at least 20 striations in more than three different locations of each condition). Although the fracture surface looks locally rounded by the formation of MVs or dimples at a lower magnification, when magnified to a certain level as in Fig. 8(d), the fatigue striations show sharp edges between each other. The fracture surface between the striations looks locally flat, but the global view still shows a significant deformation. All the observed striations are almost perpendicular to the global FCG direction. Fracture along boundaries (IG/ interfacial fracture) can be found by highly magnified images in some places. It worth mentioning that the intention of showing Fig. 8(d) is primarily a discussion on the appearance of fatigue striations. More examples of the boundary fracture can be found in Fig. A1 in the supplementary files.

3.4. Plastic deformation structure near the crack wake

Crack wake, and therefore the plastic zone was next investigated in the areas adjacent to the fracture surface of the specimens.

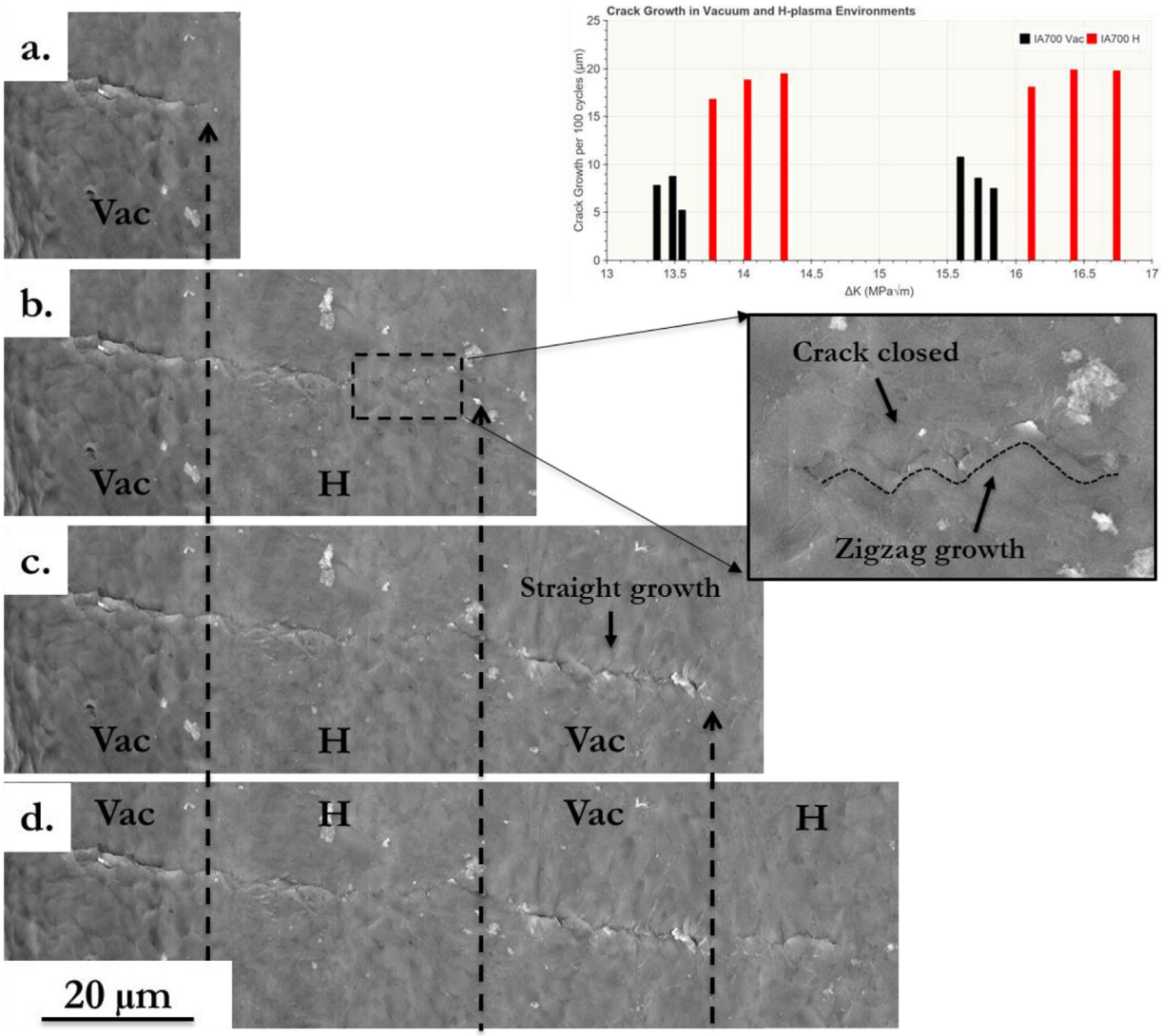

Fig. 5. Long-term crack morphology observation of IA700. The crack growth data from the presented region is shown in the bar chart. The global FCG direction is from left to right. The figures are stitched to show the crack growth history.

The microstructures are shown in Figs. 9 and 10 for IA555 and IA700, respectively. For ECC images, the varying contrast indicates a change in composition (different phases) or crystallographic orientation (plastic deformation). For the IA555 sample (Fig. 9(a) and (b)), the elongated α - γ alternative structure can be seen for both cases in the overview images. The elongated phase is roughly perpendicular to the global FCG direction, and the morphologies are similar between the two cases. A slight difference can be seen in the non-elongated phase that the contrast is varying a lot in the area close to the fracture surface in the Vac case (Fig. 9(a)), while the contrast is relatively more stable in the H case (Fig. 9(b)). This indicates that the plastic strain in the H case was weaker than the case in Vac. The plastic deformation of IA555 in terms of grain reference orientation deviation distribution can be found in Fig. A2 in the supplementary files. When taking a closer look at the deformation structures, in the Vac case, the α grains have a strong tendency to form sub-grains with scattered dislocation lines near the sub-grain boundaries (Fig. 9(c)). While in the H case, only a limited number of α grains have sub-grains and the dislocation density appears lower than that in the Vac case. The sub-grain boundaries are also thinner and sharper than that in the Vac case (Fig. 9(d)). No significant sub-structures but only dislocations are observed in the γ grains for both Vac and H cases. The high dislocation density inside the (previous) γ grains indicates a γ-α' phase transformation similar as was observed in [36].

Fig. 10 shows the same investigation on the IA700 specimen. Similarly, a relatively severe plastic deformation is observed near the fracture surface from the Vac case, in the form of distorted grains and strongly varying contrast in the overview in Fig. 10(a). On the contrary, when happened in the hydrogen environment, the nearby grains could roughly keep their shapes, and the relatively stable contrast inside grains indicates a less plasticity accumulation, as shown in Fig. 10(b). The plastic deformation of IA700 in terms of grain reference orientation deviation distribution can be found in Fig. A3 in the supplementary files. When observed at higher magnifications, the Vac case shows highly deformed structures with distorted grains and highly tangled dislocations in both α and γ/α' phases (Fig. 10(c)). In contrast, the grains more or less remained their original shapes in the H case and an interesting fact is that the dislocations have a higher tendency to accumulate at the α-γ/α' phase boundaries (Fig. 10(d)). The grain interior, on the other hand, has a relatively lower dislocation density and thus a less variation in the ECC contrast. The dislocation entanglement is also not as severe as in the Vac case. The microstructure of unde-

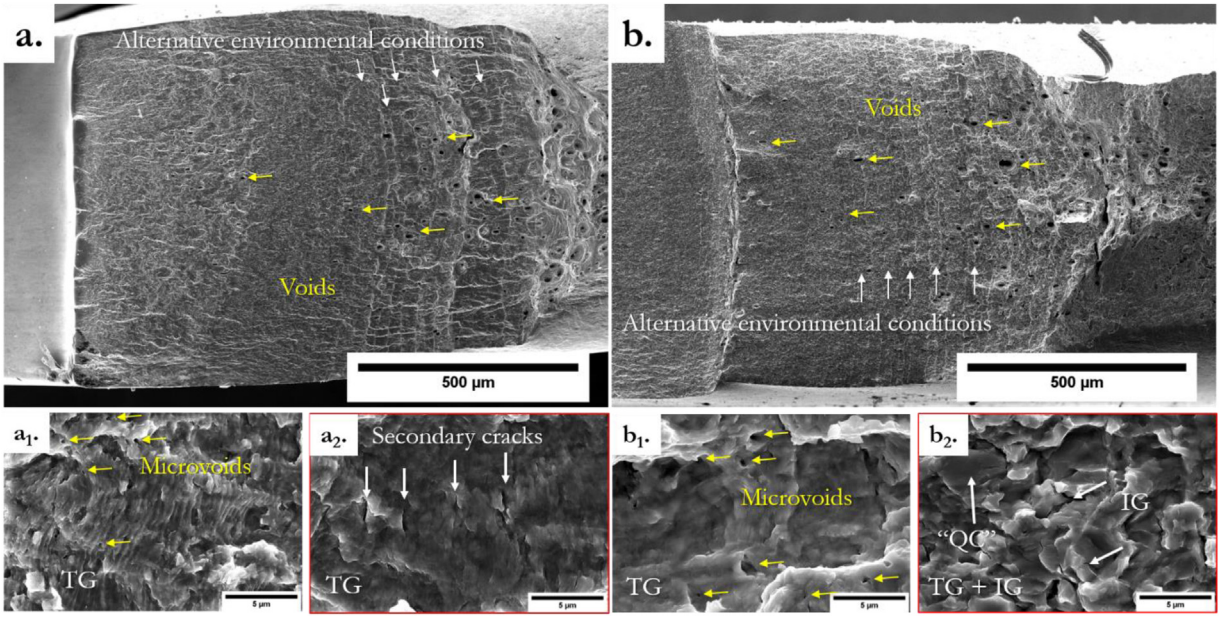

Fig. 6. Fractographs in an overview of the tested specimens: (a) IA555; (b) IA700. The global FCG direction is from left to right. The white arrows indicate the fracture features in alternative Vac and H environments. The yellow arrows indicate the dimple/ void structures. (a_1) and (b_1) are showing the typical magnified features in the regions fractured in the Vac environment of a and b, respectively. (a_2) and (b_2) are showing the typical magnified features in the regions fractured in the H environment of (a) and (b), respectively. (TG: transgranular; IG: intergranular; "QC": "quasi-cleavage") (digital version in color).

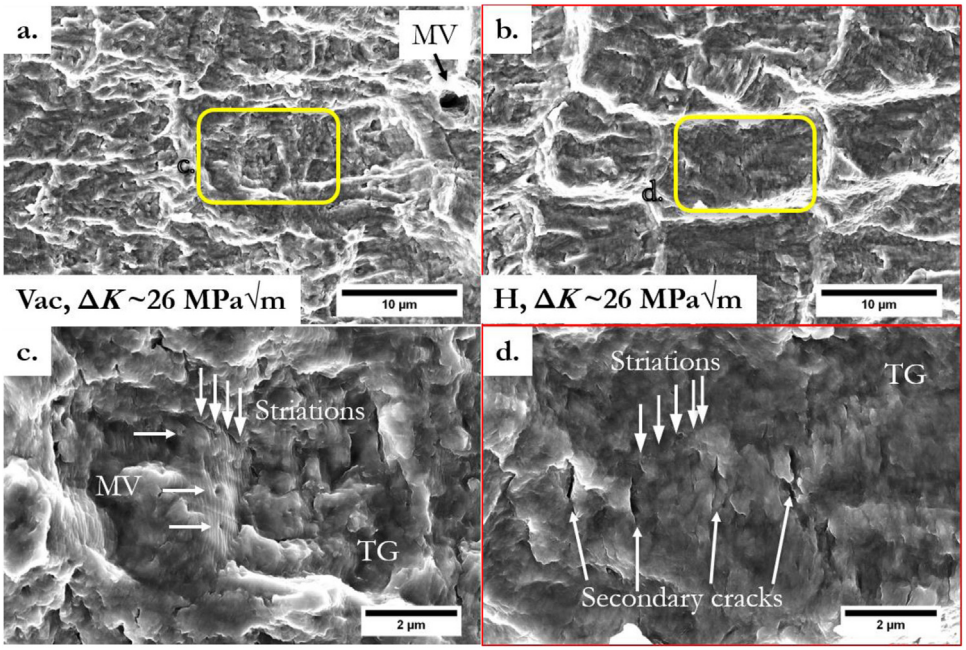

Fig. 7. Fractography of the IA555 specimen. (a) in Vac; (b) in H; (c) and (d) are the magnified areas marked in (a) and (b), respectively. The global FCG direction is from left to right. The environmental condition and the ΔK level are marked accordingly. (MV: microvoid; TG: transgranular) (digital version in color).

formed regions has been observed and shown by Figure A4 in the supplementary files. Without deformation or fracture, the γ grains contained a large number of stacking faults and annealing twins.

4. Discussion

4.1. Mechanical performance

The mechanical performance (FCG data) of the present study is revealed by the Paris' law as shown in Fig. 2 and Table 2. Since a pre-crack has been initiated before the main tests, the results are focusing on the stage II crack growth, i.e. stable crack growth regime, and the crack initiation procedure will not be discussed in the current work. Without hydrogen-charging, the FCGR curves of IA555 and IA700 are in a similar range, especially at high ΔK values, the two curves in Vac are approaching each other. In the low ΔK range, both the residual deformation from pre-cracking and the crack blunting effect after the pre-cracking can give rise to some deviations in the crack growth behavior of the investigated specimens during the *in-situ* testing. Consequently, the FCGR curves at a higher ΔK range were less influenced by the previous treatments and thus a similar FCGR behavior can be concluded for the

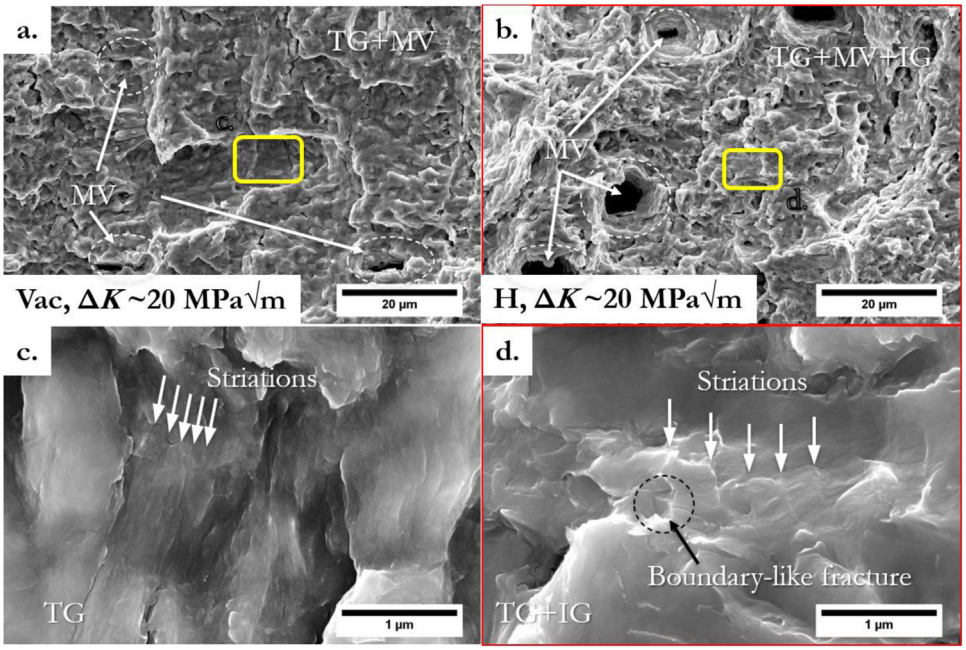

Fig. 8. Fractography of the IA700 specimen. (a) in Vac; (b) in H; (c) and (d) are the magnified areas marked in (a) and (b), respectively. The global FCG direction is from left to right. The environmental condition and the ΔK level are marked accordingly. More proof of the boundary-like fracture features can be found in supplementary files. (MV: microvoid; TG: transgranular; IG: intergranular) (digital version in color).

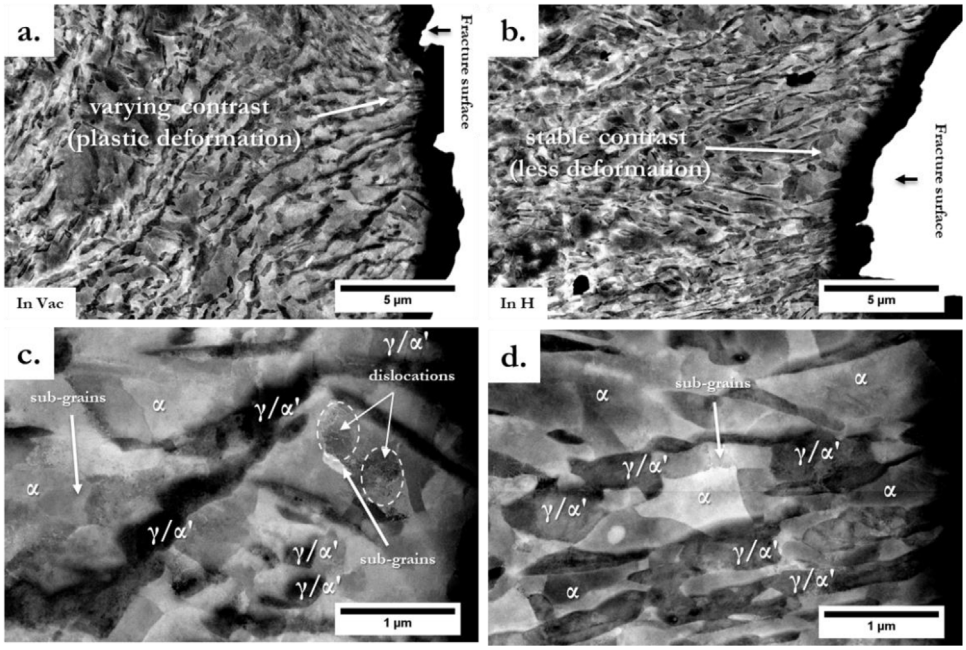

Fig. 9. ECC images of the areas immediately connecting the crack growth path in the IA555 specimen. (a) and (b) overview in Vac and H, respectively. (c) and (d) are the magnified view of (a) and (b), respectively. The global FCG direction is from top to bottom. The global ΔK level is about 26 MPa $m^{1/2}$ for all subfigures.

IA555 and the IA700 specimens without hydrogen-charging. When hydrogen was *in-situ* charged, both the IA555 and the IA700 specimens showed an acceleration in the FCGR, but the degree of such acceleration was much higher for the IA700 sample. This reflects a lower resistance to hydrogen-assisted crack propagation for the IA700 sample, compared with IA555.

Several microstructural contributions can be considered in this hydrogen embrittlement susceptibility. The IA555 material has ~40% γ phase and ~60% α phase, and the IA700 material has ~60% γ phase and ~40% α phase. The difference in the amount of phases can significantly influence the global hydrogen diffusion and distribution in the specimen since hydrogen has strongly different solubility (atomic solubility in γ about 10^{-6}-10^{-5} [64–66]; atomic solubility in α about 10^{-8}-10^{-7} [67,68]) and diffusivity (in γ about 10^{-16} m^2/s [69–71]; in α about 10^{-9}-10^{-7} m^2/s [18,72,73]) in these two crystal structures. These fundamental properties would lead to a different hydrogen distribution within the final specimens. Upon monotonic loading, hydrogen can enhance the local plastic flow in α and increase the strain incompatibility between α and the adjacent γ or α' matrix, or by being trapped at phase and grain boundaries, the decohesion effect becomes dominant that embrittles the material [36]. This can be considered as the microstructure-driven

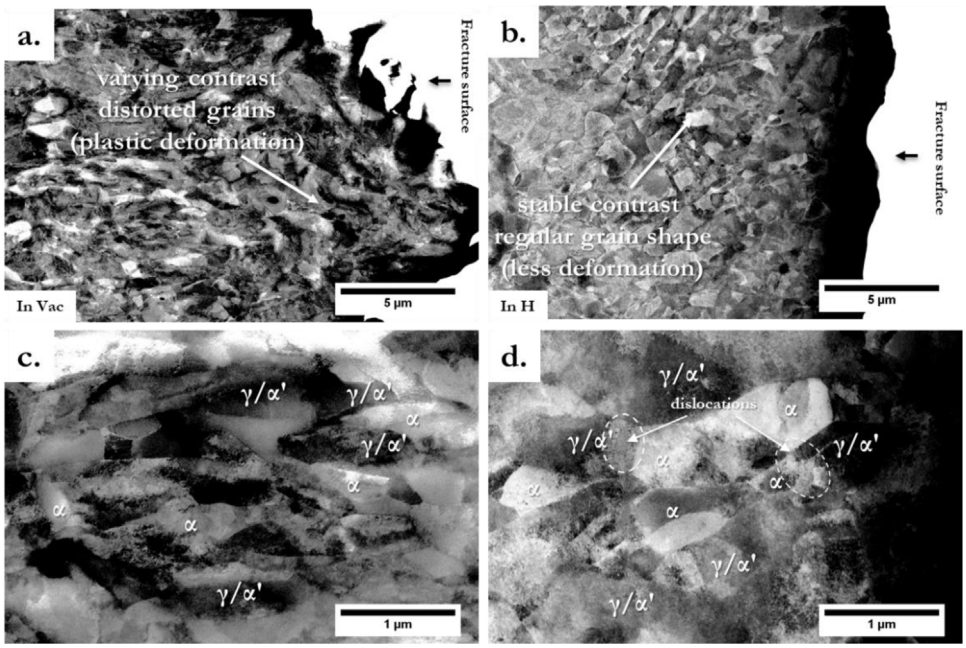

Fig. 10. ECC images of the areas immediately connecting the crack growth path in the IA700 specimen. (a) and (b) Overviews in Vac and H, respectively. (c) and (d) are the magnified view of (a) and (b), respectively. The global FCG direction is from top to bottom. The global ΔK level is about 20 MPa $m^{1/2}$ for all subfigures.

hydrogen distribution contribution to the hydrogen embrittlement susceptibility.

Another factor is the stability of the γ phase. According to [36], the stability of γ can lead to different hydrogen trapping behaviors as well as different strain-induced martensite transformation behaviors. The relatively lower γ phase fraction in IA555 (in comparison with IA700) gives relatively higher thermal and mechanical stability of the γ phase due to the C and Mn partitioning into the γ phase (as confirmed by numerical and experimental methods in [39,63]). As a result, the γ phase in IA700 has a higher probability of transforming into α'-martensite. Although the γ phase has a lower diffusivity of hydrogen, the transformed α'-martensite can act as a faster "channel" for the hydrogen transportation and finally lead to the embrittlement susceptibility in the γ-α interfaces [36]. Due to the relatively faster hydrogen diffusion in α and α' phases, it is reasonable to emphasize that *in-situ* hydrogen charging is necessary in the hydrogen embrittlement study of materials with such phases.

Furthermore, the morphology of the different phases may also give a contribution to the mechanical performance of the investigated materials. The IA555 has mainly elongated grains which lie with the elongated direction more or less perpendicular to the FCG direction, while the IA700 has mainly fully recrystallized equiaxed grains. One factor is the morphology-dependence of the stress distribution. As is from general mechanical tests, the interfaces (grain boundaries/ phase boundaries) are the possible preferential sites for stress concentration. The elongated morphology can affect the stress field in the crack wake and further affect the local hydrogen-distribution. According to the microstructure-driven hydrogen distribution in medium-Mn steels [36], the γ-α phase boundaries are a preferred trapping site for hydrogen and the hydrogen-assisted cracking will be confined close to the phase boundaries. Since the phase boundaries are mostly perpendicular to the global FCG direction in the IA555 specimen, the embrittlement susceptibility is not as high as in the IA700 specimen, which has random phase boundary distributions in the matrix. From Figs. 4 and 5, it can be seen that the fatigue crack path was not much influenced by the grain and phase boundaries in both materials in Vac; while in hydrogen, the crack path almost remained unchanged in IA555, but strongly deflected in IA700 to an IG-like morphology (this will be discussed in Section 4.2 and can be interpreted by Fig. A1 in the supplementary files). This agrees with the above-mentioned proposal. To further confirm this point, another possibility is to have the specimens cut from the same IA555 material in another direction (making the tensile direction perpendicular to the elongated direction of the grains) and perform the same test. An ideal outcome would be a more significant enhancement in the hydrogen-assisted FCGR. This will be a future work.

As a short summary, the hydrogen-assisted FCG behavior of the two medium-Mn steels in the current study could have been influenced by three factors, i.e.: microstructure-driven hydrogen diffusion (local hydrogen content and distribution); stability of the γ phase; and the morphology of the microstructure.

4.2. Failure modes

To speculate the micro-mechanism of the FCG behavior, fractography at high magnifications can be a proper and straightforward approach. As shown in Figs. 6–8, the hierarchical fracture features are presented for the investigated specimens under different loading conditions. In the overview, both IA555 and IA700 have an apparent FCG mechanism of void coalescence, shown by the voids highlighted by the yellow arrows in Fig. 6. The overall fatigue fracture features are dimple-like ductile features, indicating a relatively good ductility of the studied materials in the current testing conditions. When observed at higher magnifications in Figs. 7 and 8, the fracture surfaces of both materials in Vac show clear ductile morphology with micro-voids and parallel fatigue striations approximately perpendicular to the global FCG direction. The classical explanation of the fractographic fatigue striations (e.g. by Laird et al. [74]) comes from the consequence of alternative dislocation emission and the following slip in the fatigue crack tip region. Consequently, a residual plastically deformed region is expected in the crack wake region. Following this idea, it is natural to consider that if the dislocation slip is reversible during a single loading-unloading cycle, the crack propagation would be slower; while if the slip is irreversible, the propagated crack path would be remained permanently and thus the global FCGR would be somehow increased.

In a previous study on pure ferritic (single phase) steels with the same experimental setup by some of the present authors [47], the introduction of hydrogen plasma restricted the plastic deformation zone in the crack wake and enhanced the global FCGR. Similarly, in the dual-phase medium-Mn steels in the present work, a restricted plastic deformation zone, as well as an enhanced FCGR, has also been observed in the hydrogen environment. Considering the idea of hydrogen-restricted plastic deformation, in the H cases, the dislocations have a higher barrier against the reversible slip in the unloading half-cycles and accordingly, the stress intensity applied at the crack tip could not be released so easily as in the Vac case, and therefore, the effective K and ΔK level could have been "imaginarily increased" due to the above-mentioned irreversible dislocation motion. In fact, the cyclic slip irreversibility concept was proposed more than 10 years ago (e.g. by Mughrabi [75]), but this mechanism has been generally used to explain the surface damages such as extrusions/intrusions in fatigue loading. Considering the fatigue crack tip is a surface defect and the FCG propagation is the accumulation of the damages produced from each loading cycle, the restrictive effect from hydrogen on the plastic deformation can be used as a factor enhancing the dislocation slip irreversibility. This explanation is in good agreement with the present results.

Another possible way to explain this behavior would be from the energy point of view. Assuming the amount of work done by the external loading in one cycle is roughly a fixed amount, this part of the energy will be released by the material either by plastic deformation or opening of atomic planes/ decohesion of boundaries (considered as elastic opening without residual plastic deformation). Normally, the plastic deformation is making the crack tip blunt and the elastic opening of atomic planes/ boundaries is making the crack grow longer. If the plastic deformation in the crack tip region is restricted, this part of energy output would also be reduced, and consequently, the energy consumed in the elastic opening of atomic planes/ boundaries would be enhanced. The distance between the fatigue striations in the H case can be larger than that in the Vac case and the appearance of the fracture surface would be flatter and less (plastically) strained. This agrees well with the fractographic observations in Figs. 7 and 8. If a weak boundary is encountered by the crack tip in the H case, the decohesion of the boundary can also give contribution to the energy relief and a boundary-like fracture feature would be expected on the fractographs, as experienced by the IA700 specimen highlighted in Fig. 8d. In contrast to IA700, the fractographic fatigue striations in IA555 do not have the same sharp appearance but rather look like deeper secondary cracks. One possible explanation is that since the grains are in elongated morphologies, the phase and grain boundaries are generally perpendicular to the global FCG direction. When looking on the fracture surfaces, these boundary planes are perpendicular to the paper plane (roughly the fracture surface plane). As discussed in the previous section and according to the hydrogen distribution scheme in Ref. [36], the phase boundaries are preferred hydrogen concentrated regions, where boundary decohesion likely happens. As a consequence, the decohered boundaries open into the matrix material and appear as secondary cracks on the fracture surface as in Fig. 7(d). The distance between the striations of about 2 μm corresponds well to the interphase distances in IA555 as shown in Fig. 3(a) and (b). This type of boundary decohesion can balance the energy consumption as stated above, however, the contribution to the primary fatigue crack propagation is rather limited due to the spatial distribution of the cracks. This is well in accord with the mechanical performance that under the same hydrogen charging conditions, the enhancement of the FCGR is more significant in IA700 than in IA555 (Fig. 2 and Table 2).

4.3. Hydrogen influence on the deformation and FCG mechanisms

Summarizing each of the simple cases discussed above, the overall picture of the FCG behavior in the studied medium-Mn steels becomes more and more clear. Fig. 11 shows a schematic of the proposed mechanisms. In the hydrogen-free case, both IA555 and IA700 show straightforward TG FCG behavior (Fig. 11(a) and (c)). The microstructural differences in the two materials do not give significant contribution to the FCG properties and the FCGR is mainly controlled by the external loading (ΔK level) and follows the Paris' law. A relatively large residual plastic deformation zone is expected near the crack wake. When the hydrogen environment is applied, a different FCG behavior is foreseen in the two materials. In IA555 (Fig. 11(b)), the hydrogen would restrict the plastic deformation zone to a region closer to the crack and the FCGR would be faster than the Vac case. Secondary cracks are expected mainly along some γ-α phase boundaries, but since most of the boundaries are perpendicular to the primary FCG direction, the main fatigue fracture does not follow the boundary morphology. Therefore, the expected primary FCG path is still straightforward, but with some secondary branches. In IA700 (Fig. 11(d)), a similar hydrogen-restricted plastic deformation zone as well as enhanced FCGR would be expected, but the crack path would appear more in an IG way that mainly follows the γ-α phase boundaries.

The most influencing factor comes from the response of different phases (γ, α and α') to hydrogen. The hydrogen adsorption, absorption, migration, trapping and the final distribution in the material are strongly dependent on the phases. As stated in Section 4.1, hydrogen has a low diffusivity and high solubility in the γ phase, while a high diffusivity and low solubility in the α phase. It is expected that the hydrogen is mainly migrating in the α grains but will be attracted by the γ phase. If the environmental hydrogen is continuously provided (the current testing condition), the α grains will be expected to have a supersaturation of hydrogen, and the γ-α phase boundaries would be a preferred hydrogen concentrated region. Therefore, the most significant embrittlement behavior happens in the phase boundary regions and varies depending on the microstructural distribution of the phases. Considering the mechanical stability of γ phases, a different α' fraction near the crack wake should also be discussed. From previous studies, the γ phase in medium-Mn steels is metastable and can transform into α' easily near the crack wake [2,6,7,33,35–41]. In the current study, IA555 has more stable γ phases than IA700 and thus the α' phase transformation is more significant in IA700. This phase distribution makes the hydrogen diffusion much deeper in the IA700 case due to a larger fraction of α' near the crack path. Furthermore, the IA700 materials have a macroscopically lower yielding strength than IA555 ($\sim$426 $\pm$ 14 MPa in IA700 vs. $\sim$899 $\pm$ 15 MPa in IA555 [2]). Considering a similar stress intensity level, the plastic deformation in IA700 should be more significant and thus the deformation-induced α' transformation is expected to be deeper in IA700 than in IA555. As a short summary, the α'-influenced hydrogen distribution can be an important factor contributing to the different hydrogen-assisted FCG behavior in the current study.

Moreover, the synergistic effect of different hydrogen embrittlement mechanisms can also play an important role in the current study. As summarized in literature, the HELP and HEDE mechanisms can occur both individually and simultaneously based on the local hydrogen concentration, which can be described by HELP + HEDE synergy and/ or HELP-mediated HEDE models [24,76]. Based the current results, the HELP and HEDE synergy can be characterized by the mixed fracture mode of MV + TG + microcracks in IA555 (Fig. 7) and of MV + TG + IG in IA700 (Fig. 8) [76].

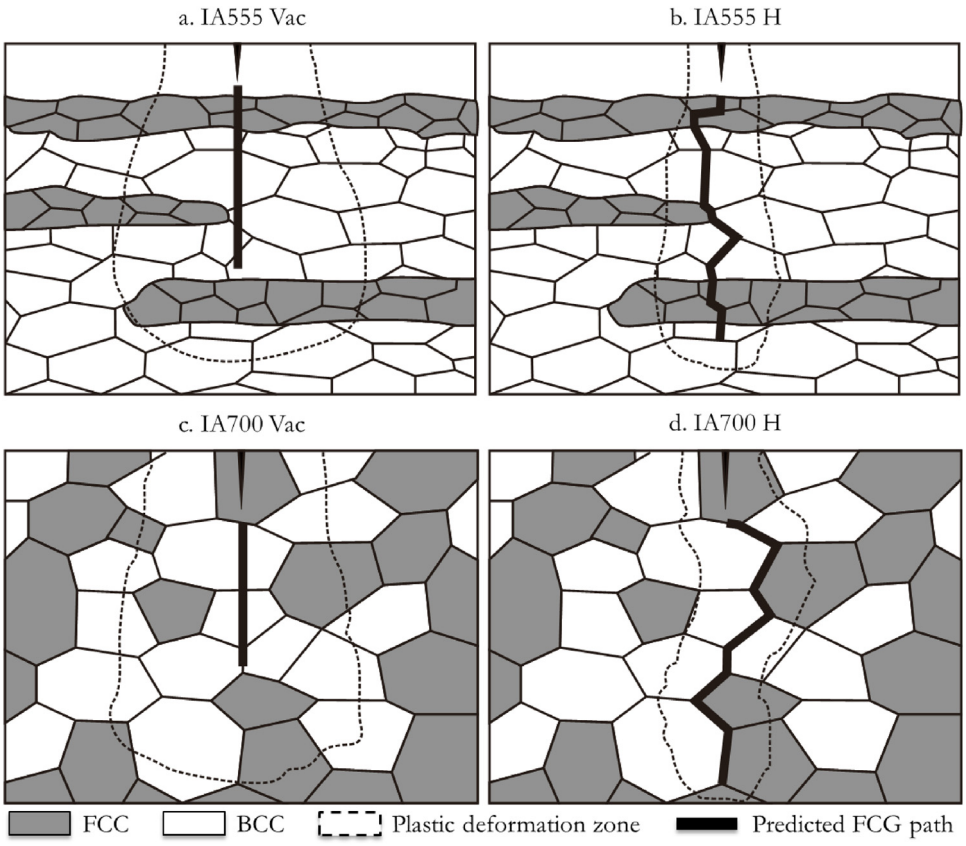

Fig. 11. Proposed FCG mechanism of the studied medium-Mn steels in different environmental conditions.

The appearance of the hydrogen-induced "QC" features in IA700 reflects the HELP-mediated-HEDE model, since the "QC" fracture happens as a result of dislocation pile-ups impinging on block boundaries. The IG fracture in the H cases can be explained as a combined effect of a weakened boundary cohesion energy by the HEDE mechanism and an additional stress field concentrated at the boundaries by the dislocation pile-ups' stress due to the HELP mechanism [26]. These synergistic actions of different hydrogen embrittlement mechanisms have been well summarized and validated in different materials by experimental proofs [25,28–30], and a quantitative model has been built to describe the behavior [27].

Nevertheless, the proposed mechanism in Fig. 11 is an idealized and simplified model that needs further careful calibration when describing a complex real case. In the current study, the introduction of hydrogen plasma increased the FCGR of both the IA555 and the IA700 materials with a different factor (up to 2 times). A noteworthy point here is that the FCGR is a global behavior that is contributed by other mechanisms from micro- to macro-scales as well. The relatively mild environment of hydrogen plasma had a visible change in the crack path, plastic deformation zone closes to the crack as well as the fractography (Figs. 2–10), but in comparison with the basic FCGR data obtained from Vac, this degradation does not seem to be as surprising as from other conventional approaches. However, since the current study is focusing on the mechanism of the hydrogen-assisted FCGR behavior of the studied materials, the present results could be a reasonable outcome.

The pity here is the lack of accurate estimation of the hydrogen distribution in such a complex microstructure [36]. The currently available techniques are mostly based on thermal desorption analysis (TDA), which can roughly give the hydrogen concentration by detecting the hydrogen output upon increasing the temperature of a specimen. The possible trapping sites of hydrogen in the complex UFG microstructured materials lead to a wide range of thermal desorption, which will be challenging to be accurately analyzed. Furthermore, due to the fast diffusion of hydrogen in BCC phases, the time between the charging and the TDA will also strongly influence the results. The hydrogen-influenced region in the current study is in the magnitude of several microns, and the out-diffusion of hydrogen in the α phase needs a time interval in the magnitude of 10^{-2} s after simplified diffusion calculation. A reliable and *in-situ* technique that can detect hydrogen with high spatial resolution in the nanometer scale is needed for accurate hydrogen embrittlement study in complex microstructures. According to literature, scanning Kelvin prove force microscopy and atom probe tomography can be the candidate techniques in the future studies [77]. Another possibility is atomic scale simulations such as density function theory (DFT) [78–80]. However, the techniques are not available in the authors' current institution and the numerical method is not the study field of the authors. The readers who have the ability and who are interested in continuing these studies are encouraged to contact the corresponding author of this paper for future collaborations.

5. Conclusions

A refined study focusing on the FCG behavior has been conducted on two SENT specimens from a medium-Mn steel with different microstructures, respectively, in alternative vacuum - hydrogen plasma environments. Both *in-situ* and *ex-situ* SEM investigations have been used to explore the mechanism of hydrogen-assisted FCG procedure in medium-Mn steels. Some conclusions can be drawn as follows:

(1) The hydrogen plasma has an effect of slightly promoting FCGR of the studied medium-Mn steel with different microstructures (IA555 and IA700 conditions), giving an accelerating factor of about 1.7 times for IA555 and about 2 times for IA700.
(2) A clear transition in the fractography (from ductile striations to brittle-like striations/ IG fractures) can be observed for both materials.
(3) A restricted plastic deformation zone is observed close to the fracture surface of both specimens.
(4) The mixed fracture modes (TG + IG/ TG + microcracks/ TG + IG + MV) appeared in the H cases indicate a synergistic action of multiple hydrogen embrittlement mechanisms such as HELP + HEDE and HELP-mediated-HEDE models.
(5) IA700 shows a slightly lower resistance to the hydrogen-assisted FCG due to its higher γ fraction (~60% γ in IA700 vs. ~40% γ in IA555), lower γ stability and lower yielding strength in comparison with IA555.
(6) IA700 has a higher possibility of crack propagation along boundaries than IA555, possibly due to the microstructure-driven hydrogen diffusion and redistribution.

Acknowledgements

This work has been financially supported by the Department of Mechanical and Industrial Engineering (MTP), Norwegian University of Science and Technology (NTNU). The authors gratefully acknowledge the financial support of the Deutsche Forschungsgemeinschaft (DFG) within the Collaborative Research Center (SFB) 761 “Steel-ab initio: Quantum mechanics guided design of new Fe-based materials”. Encouragement from Prof. Afrooz Barnoush at MTP, NTNU is gratefully acknowledged.

Appendix A. Supplementary data

Supplementary material related to this article can be found, in the online version, at doi:https://doi.org/10.1016/j.jmst.2020.12.069.

References

[1] Y. Ma, Mater. Sci. Technol. 33 (2017) 1713–1727.
[2] Y. Ma, W. Song, S. Zhou, A. Schwedt, W. Bleck, Metals 8 (2018) 357.
[3] D.K. Matlock, J.G. Speer, Microstructure and Texture in Steels 2009, London, 2009, pp. 185–205.
[4] B. Sun, F. Fazeli, C. Scott, S. Yue, Metall. Mater. Trans. A 47 (2016) 4869–4882.
[5] B.B. He, H.W. Luo, M.X. Huang, Int. J. Plast. 78 (2016) 173–186.
[6] B.B. He, M.X. Huang, Metall. Mater. Trans. A 47 (7) (2016) 3346–3353.
[7] I. Jeong, K.M. Ryu, D.G. Lee, Y. Jung, K. Lee, J.S. Lee, D.-W. Suh, Scr. Mater. 169 (2019) 52–56.
[8] W.H. Johnson, Proc. R. Soc. Lond. 23 (1875) 168–179.
[9] R.A. Oriani, Acta Metall. 18 (1970) 147–157.
[10] R.A. Oriani, P.H. Josephic, Acta Metall. 25 (1977) 979–988.
[11] W.W. Gerberich, R.A. Oriani, M.J. Lji, X. Chen, T. Foecke, Philos. Mag. A 63 (1991) 363–376.
[12] C.D. Beachem, Metall. Mater. Trans. B 3 (1972) 441–455.
[13] I.M. Robertson, H.K. Birnbaum, Acta Metall. 34 (1986) 353–366.
[14] H.K. Birnbaum, P. Sofronis, Mater. Sci. Eng. A 176 (1994) 191–202.
[15] I.M. Robertson, Eng. Fract. Mech. 68 (2001) 671–692.
[16] S.P. Lynch, Acta Metall. 36 (1988) 2639–2661.
[17] S.P. Lynch, Scr. Mater. 61 (3) (2009) 331–334.
[18] S. Lynch, Corros. Rev. 30 (2012) 105–123.
[19] M. Nagumo, Mater. Sci. Technol. 20 (2004) 940–950.
[20] O. Barrera, D. Bombac, Y. Chen, T.D. Daff, E. Galindo-Nava, P. Gong, D. Haley, R. Horton, I. Katzarov, J.R. Kermode, C. Liverani, M. Stopher, F. Sweeney, J. Mater. Sci. 53 (2018) 6251–6290.
[21] R. Kirchheim, Int. J. Mater. Res. 100 (2009) 483–487.
[22] R. Kirchheim, Scr. Mater. 62 (2010) 67–70.
[23] R. Kirchheim, Scr. Mater. 67 (2012) 767–770.
[24] M.B. Djukic, G.M. Bakic, V. Sijacki Zeravcic, A. Sedmak, B. Rajicic,Eng. Fract. Mech. 216 (2019), 106528.
[25] M.L. Martin, M. Dadfarnia, A. Nagao, S. Wang, P. Sofronis, Acta Mater. 165 (2019) 734–750.
[26] A. Nagao, M. Dadfarnia, B.P. Somerday, P. Sofronis, R.O. Ritchie, J. Mech. Phys. Solids 112 (2018) 403–430.
[27] P. Novak, R. Yuan, B.P. Somerday, P. Sofronis, R.O. Ritchie, J. Mech. Phys. Solids 58 (2010) 206–226.
[28] B.N. Popov, J.-W. Lee, M.B. Djukic, Handbook of Environmental Degradation of Materials, third ed., 2018, pp. 133–162.
[29] J. Rehrl, K. Mraczek, A. Pichler, E. Werner, Mater. Sci. Eng. A 590 (2014) 360–367.
[30] D. Sasaki, M. Koyama, H. Noguchi, Mater. Sci. Eng. A 640 (2015) 72–81.
[31] M.B. Djukic, G.M. Bakic, V.S. Zeravcic, A. Sedmak, B. Rajicic, Corrosion 72 (2016) 943–961.
[32] J.H. Ryu, Y.S. Chun, C.S. Lee, H.K.D.H. Bhadeshia, D.W. Suh, Acta Mater. 60 (2012) 4085–4092.
[33] J. Han, J.-H. Nam, Y.-K. Lee, Acta Mater. 113 (2016) 1–10.
[34] X. Lu, Y. Ma, M. Zamanzade, Y. Deng, D. Wang, W. Bleck, W.W. Song, A. Barnoush, Int. J. Hydrogen Energy 44 (2019) 20545–20551.
[35] X. Shen, W. Song, S. Sevsek, Y. Ma, C. Hüter, R. Spatschek, W. Bleck, Metals 9 (2019) 929.
[36] B. Sun, W. Krieger, M. Rohwerder, D. Ponge, D. Raabe, Acta Mater. 183 (2020) 313–328.
[37] X. Li, R. Song, N. Zhou, J. Li, Scr. Mater. 154 (2018) 30–33.
[38] B. Sun, R. Ding, N. Brodusch, H. Chen, B. Guo, F. Fazeli, D. Ponge, R. Gauvin, S. Yue, Mater. Sci. Eng. A 749 (2019) 235–240.
[39] B. Sun, F. Fazeli, C. Scott, B. Guo, C. Aranas, X. Chu, M. Jahazi, S. Yue, Mater. Sci. Eng. A 729 (2018) 496–507.
[40] B. Sun, F. Fazeli, C. Scott, X. Yan, Z. Liu, X. Qin, S. Yue, Scr. Mater. 130 (2017) 49–53.
[41] S. Lee, B.C. De Cooman, Metall. Mater. Trans. A 44 (11) (2013) 5018–5024.
[42] B.H. Sun, D. Palanisamy, D. Ponge, B. Gault, F. Fazeli, C. Scott, S. Yue, D. Raabe, Acta Mater. 164 (2019) 683–696.
[43] T.L. Anderson, Fracture Mechanics: Fundamentals and Applications, third ed., CRC Press, Boca Raton, 2005.
[44] C.G. Morgan, R. Vane, Removal of Carbon Contamination Using Hydrogen With Low-power Downstream Plasma Cleaning, 2011 https://evactron.com/wp-content/uploads/2016/10/cleaningwithh2advlith2011.pdf.
[45] G.M. Bond, I.M. Robertson, H.K. Birnbaum, Scr. Metall. Mater. 20 (1986) 653–658.
[46] D. Wan, Y. Deng, A. Barnoush, Scr. Mater. 151 (2018) 24–27.
[47] D. Wan, Y. Deng, J.I.H. Meling, A. Alvaro, A. Barnoush, Acta Mater. 170 (2019) 87–99.
[48] T. Depover, T. Hajilou, D. Wan, D. Wang, A. Barnoush, K. Verbeken, Mater. Sci. Eng. A 754 (2019) 613–621.
[49] A. Alvaro, D. Wan, V. Olden, A. Barnoush, Procedia Struct. Integr. 13 (2018) 1514–1520.
[50] A. Alvaro, D. Wan, V. Olden, A. Barnoush,Eng. Fract. Mech. 219 (2019), 106641.
[51] D. Wan, A. Alvaro, V. Olden, A. Barnoush, Hydrogen-assisted fatigue crack growth in ferritic steels – a fractographic study, MATEC Web of Conferences (2018) 03004.
[52] D. Wan, A. Alvaro, V. Olden, A. Barnoush, Int. J. Hydrogen Energy 44 (2019) 5030–5042.
[53] Y. Ogawa, D. Birenis, H. Matsunaga, O. Takakuwa, J. Yamabe, Ø. Prytz, A. Thøgersen, MATEC Web of Conferences, 165, 2018, pp. 03011.
[54] D. Birenis, Y. Ogawa, H. Matsunaga, O. Takakuwa, J. Yamabe, Ø. Prytz, A. Thøgersen, MATEC Web of Conferences, 165, 2018, pp. 03010.
[55] D. Birenis, Y. Ogawa, H. Matsunaga, O. Takakuwa, J. Yamabe, Ø. Prytz, A. Thøgersen, Acta Mater. 156 (2018) 245–253.
[56] G. Bilotta, G. Henaff, D. Halm, M. Arzaghi, Int. J. Hydrogen Energy 42 (2017) 10568–10578.
[57] S.M. Myers, M.I. Baskes, H.K. Birnbaum, J.W. Corbett, G.G. DeLeo, S.K. Estreicher, E.E. Haller, P. Jena, N.M. Johnson, R. Kirchheim, S.J. Pearton, M.J. Stavola, Rev. Mod. Phys. 64 (1992) 559–617.
[58] S. Zaefferer, N.N. Elhami, Acta Mater. 75 (2014) 20–50.
[59] D. Wan, A. Barnoush, Mater. Sci. Eng. A 744 (2019) 335–339.
[60] B.H. Sun, Y. Ma, N. Vanderesse, R.S. Varanasi, W.W. Song, P. Bocher, D. Ponge, D. Raabe, Acta Mater. 178 (2019) 10–25.
[61] P. Paris, F. Erdogan, J. Basic Eng. 85 (4) (1963) 528–533.
[62] B. Sun, N. Vanderesse, F. Fazeli, C. Scott, J. Chen, P. Bocher, M. Jahazi, S. Yue, Scr. Mater. 133 (2017) 9–13.
[63] B.H. Sun, F. Fazeli, C. Scott, N. Brodusch, R. Gauvin, S. Yue, Acta Mater. 148 (2018) 249–262.
[64] A. Turnbull, R.B. Hutchings, Mater. Sci. Eng. A 177 (1-2) (1994) 161–171.
[65] E.J. Song, H.K.D.H. Bhadeshia, D.-W. Suh, Corros. Sci. 77 (2013) 379–384.
[66] L.C.D. Fielding, E.J. Song, D.K. Han, H.K.D.H. Bhadeshia, D.W. Suh, Proc. R. Soc. A 470 (2014) 2168.
[67] K. Kiuchi, R.B. McLellan, Acta Metall. 31 (1983) 961–984.
[68] I.M. Bernstein, Mater. Sci. Eng. 6 (1970) 1–19.
[69] D. Wang, X. Lu, Y. Deng, X. Guo, A. Barnoush, Acta Mater. 166 (2019) 618–629.
[70] D. Wang, X. Lu, D. Wan, Z. Li, A. Barnoush, Scr. Mater. 173 (2019) 56–60.
[71] V. Olden, C. Thaulow, R. Johnsen, Mater. Des. 29 (10) (2008) 1934–1948.
[72] P. Bruzzoni, R.M. Carranza, J.R. Collet Lacoste, E.A. Crespo, Electrochim. Acta 44 (1999) 2693–2704.
[73] S. Wang, N. Hashimoto, S. Ohnuki, Mater. Sci. Eng. A 562 (2013) 101–108.
[74] C. Laird, G.C. Smith, Philos. Mag. 7 (1962) 847–857.

[75] H. Mughrabi, Metall. Mater. Trans. B 40 (2009) 431–453.
[76] M.B. Djukic, V. Sijacki Zeravcic, G.M. Bakic, A. Sedmak, B. Rajicic, Eng. Fail. Anal. 58 (2015) 485–498.
[77] M. Koyama, M. Rohwerder, C.C. Tasan, A. Bashir, E. Akiyama, K. Takai, D. Raabe, K. Tsuzaki, Mater. Sci. Technol. 33 (2017) 1481–1496.
[78] D.E. Jiang, E.A. Carter, Acta Mater. 52 (2004) 4801–4807.
[79] D.E. Jiang, E.A. Carter, Phys. Rev. B 70 (2004).
[80] M. Itakura, H. Kaburaki, M. Yamaguchi, T. Okita, Acta Mater. 61 (2013) 6857–6867.